Studies of Target Implosion Using *K*-Shell Absorption Spectroscopy of an Embedded Titanium Layer

In laser-imploded target studies, the measurement of shell compression and uniformity is essential to understand target performance. Previously we have used targets in which a titanium-doped layer was incorporated into the target shell. The doped layer provided a variety of diagnostic signatures (absorption lines, *K*-edge absorption, Kα imaging) for determining the areal density and density profile of the shell around peak compression.[1–5] In this article we apply some of these methods to demonstrate the improvement in target performance when implementing SSD[6] (smoothing by spectral dispersion). In particular, we study slow-rising laser pulses (for low-adiabat implosions), where the effect of SSD smoothing is more pronounced. In addition, we introduce a new method for studying the uniformity of imploded shells: using a recently developed[5] pinhole-array x-ray spectrometer we obtain core images at energies below and above the *K*-edge energy of titanium. The nonuniformity of such images depends on the nonuniformity of both the emitting core and the absorbing shell; however, the ratio between the images above and below the *K* edge essentially depends on the nonuniformity of the shell alone. Finally, we compare the results with those of 1-D *LILAC* simulations, as well as 2-D *ORCHID* simulations, which allow for the imprinting of laser nonuniformity on the target. The experimental results are replicated much better by *ORCHID* than by *LILAC*.

Areal-Density Measurement Using *K*-Shell Absorption

To demonstrate the effect of SSD on target performance we chose two pairs of laser shots from two different series; for each pair all conditions were nearly identical except for the presence of SSD. The target and laser conditions for these shots are listed on the first four lines of Table 79.III. The two target shots with SSD are almost identical as are the two shots without SSD and they can be used interchangeably. The pulse shape in these four shots was the 2.5-ns, slow-rising pulse shape ALPHA306: starting with a flat, 0.5-ns foot at 2.5% of the peak, followed by a 1.1 ns of a slowly rising ramp, then a 0.2 ns of a faster-rising ramp, it finally reaches a 0.7-ns flat top. This pulse has been shown to place the colder part of the shell during the laser irradiation of typical CH shells on an adiabat of $\alpha \sim 3$. It is particularly suitable for studying the effect of SSD smoothing on reducing imprinting because faster-rising pulses cause early decoupling of laser and shell, which reduces the imprint even without SSD. All four targets were voided, to

Table 79.III: Experimental parameters for the laser shots discussed in this article. The first four shots demonstrate improvement in performance due to SSD; the fifth shot is discussed in the last section of this article. All shots had a Ti-doped layer embedded in the shell (atom concentration of Ti is given in brackets). ALFA306 is a slow-rising, 2.5-ns pulse shape.

Shot No.	Inner radius (μm)	Inner CD layer (μm)	CH(Ti) layer (μm)	Outer CH layer (μm)	Total shell thickness (μm)	Fill gas (atm)	2-D SSD bandwidth (Å)	Pulse shape	Laser energy (kJ)
13151	444.5	5.8	4.8 (4%)	14.3	24.9	void	1.25 × 1.65	ALFA306	21.0
13152	445.0	5.7	5.1 (4%)	14.3	25.1	void	–	ALFA306	21.7
13936	448.5	5.0	5.7 (4.3%)	15.7	26.4	void	1.28 × 1.7	ALFA306	19.5
13939	442.5	5.0	5.7 (4.3%)	15.7	26.4	void	–	ALFA306	22.6
15156	438.5	0.8	2.6 (6.2%)	16.6	20.0	DD (3)	1.26 × 1.76	1-ns square	26.2

resemble the implosion of future cryogenic targets. The structure of the targets was chosen so that the doped layer would become nearly identical with the cold layer at peak compression. The thickness of the overcoat CH layer was chosen so as to be ablated away during the laser pulse; indeed, the laser burned through it toward the end of the pulse. The inner layer was thick enough to constitute the hot, compressed core. This conclusion is based on the observation of Ti plasma lines emitted at the center of the target. In the last section we describe measurements of shell nonuniformity obtained with a different pulse shape: a 1-ns square pulse.

The x-ray spectra were recorded by a space-resolving, time-integrating spectrograph and a streak spectrograph. The first spectrograph used a Ge(111) crystal and a 25-μm-wide spatially resolving slit. The continuum core emission was clearly visible above the much-weaker radiation of larger extent from the interaction region (see Fig. 4 in Ref. 3; also, Fig. 79.28 below); thus, for measuring the absorption of core radiation within the shell, the radiation from the interaction region can be easily subtracted. The crystal calibration curve (see Fig. 4 in Ref. 1) is relatively flat in the 3- to 6-keV region. The streak spectrograph used a RbAP crystal with the image recorded on film. The sensitivity of the film is determined with a density wedge developed simultaneously with the data; however, because the photocathode is not uniformly sensitive across its surface, we used the streak data to monitor the temporal changes but the areal-density determinations relied on the time-integrated spectra. This point is further discussed below.

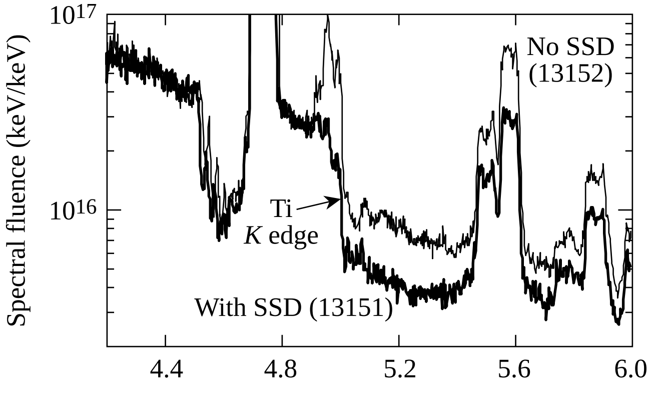

Figure 79.23
Comparison of spectra from two shots (conditions listed in Table 79.III). The main difference is the larger drop above the *K* edge of Ti (around ~ 5 keV) due to SSD smoothing, indicating a higher cold-shell areal density.

Figure 79.23 shows a comparison of the calibrated, time-integrated spectra from shots 13151 and 13152. Figure 79.24 shows lineouts through the streak spectrum for shot 13152 at three different times; the streak spectra for shot 13151 are qualitatively similar. The upper spectrum is emitted during the laser irradiation, and the lower two spectra are emitted at two instances during the compression; the complete record shows that when the laser irradiation terminates, the x-ray emission falls and then rises again during compression. For clarity, the upper curve in Fig. 79.24 was raised by 30. Figure 79.24 clearly shows that the lines of highly ionized Ti ions are emitted during the laser irradiation; their large width (in both Figs. 79.23 and 79.24) is due to source broadening, corresponding to emission from the laser-interaction region. This is also evident from the spatially resolved spectra (e.g., see Fig. 79.28 below). Figure 79.23 shows a higher intensity of these Ti lines when SSD was not implemented. This is consistent with the results of burnthrough experiments[7] that show a faster burnthrough when SSD is absent, due to a higher level of laser imprint.

Turning to the core emission, we see that continuum radiation from the imploded core (formed by the inner layer of the shell) is absorbed when traversing the cold titanium-doped layer. Two types of absorption are evident: 1*s*–2*l* absorption lines in Ti ions with successive *L*-shell vacancies (around

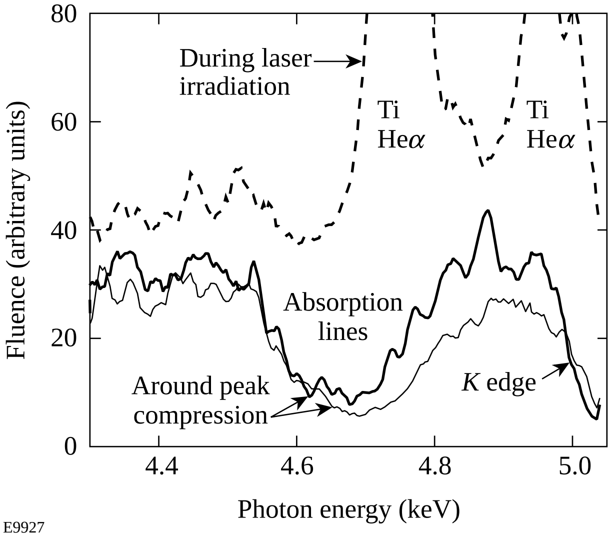

Figure 79.24
Lineouts through the streak spectrum at three different times. The upper spectrum is emitted during the laser irradiation, the lower two spectra at different instances during the compression. Ti lines are seen to be emitted during the laser irradiation. The absorption lines and *K*-edge absorption are seen to occur simultaneously. For clarity the upper curve was raised by 30.

4.6 keV) and Ti *K*-edge absorption (at ~5 keV). We show in the next section that the lines are absorbed in a layer of temperature in the range of ~200 to ~400 eV surrounding the core (the "cool" shell layer), whereas the radiation above the Ti *K* edge is absorbed in a colder layer of temperature in the range of ~150 to ~220 eV surrounding the former layer (the "cold" shell layer).

The drop in intensity across the Ti *K* edge yields the areal density of the titanium alone, using standard tables of absorption in titanium foils; calculations[8] show that at higher temperatures, when *M*- and *L*-shell electrons are successively removed, the *K* edge shifts to higher energies but at a given energy above the edge the absorption hardly changes with ionization. The intensity ratio $R_K = I\left(< E_K\right)/I\left(> E_K\right)$, where $< E_K$ means an energy just below and $> E_K$ just above the Ti *K* edge, is related to the difference in opacity $\Delta\tau = \tau\left(> E_K\right) - \tau\left(< E_K\right)$: $R_K = \exp(\Delta\tau)$. More precisely, this value is used as an initial guess in calculating the spectrum above the *K* edge before its absorption and adjusting it to join smoothly the measured spectrum below the *K* edge (see Fig. 6 in Ref. 1). For shot 13151 (with SSD) the Ti areal density is found to be 1.7 mg/cm^2, and for shot 13152 (without SSD) it is 0.78 mg/cm^2. Knowing the Ti concentration, the areal density of the cold doped layer is found to be 7.3 mg/cm^2 and 3.4 mg/cm^2, respectively. These values of $\rho\Delta R$ were obtained from the time-integrated spectra because of their higher spectral resolution as compared with the streak-spectra data; however, the streak data provide additional support for these results. During the time when the core emission is intense, the absorption seen in the streak data does not change appreciably so that the peak $\rho\Delta R$ does not exceed the average $\rho\Delta R$ by more than a factor of ~1.3. It should be noted that the background continuum emitted by the laser-interaction region is distinct from the core continuum in both time and space. Thus, in determining the continuum absorption the background can be removed through either time resolution or space resolution (see Fig. 4 in Ref. 3).

In addition to the *K*-edge absorption, the absorption lines around 4.6 keV yield the areal density of the cool region. Using the method explained in Ref. 9 and used in Ref. 1, we derive ~3.5 mg/cm^2 for the $\rho\Delta R$ of that region. The total areal density of the doped layer is the sum of the $\rho\Delta R$ derived from the *K*-edge absorption and the $\rho\Delta R$ derived from the absorption lines since, as Fig. 79.24 shows, *the two absorptions for the most part occur simultaneously*. Thus, the total areal density of the doped layer with and without SSD becomes 10.8 mg/cm^2 and 6.9 mg/cm^2, respectively. Applying a correction derived from the streak spectra, the *peak* $\rho\Delta R$ *values* are ~14 mg/cm^2 and 9 mg/cm^2, respectively. The uncertainty in these values is ±25%.

Figure 79.23 shows that, whereas the *K*-edge jump differs appreciably for the two spectra, the line absorption as well as the core continuum emission is very similar. The two are related because the lines are absorbed on the fringes of the hot core; thus, the energy dumped into the core depends more on the absorbed laser energy and less on the irradiation uniformity.

The total areal density of the compressed shell can be obtained approximately by multiplying the measured $\rho\Delta R$ of the doped layer by a factor $Q = (\rho\Delta R)_{0,\text{unablated}}/(\rho\Delta R)_{0,\text{doped}}$, where $(\rho\Delta R)_{0,\text{ unablated}}$ is the areal density of the part of the shell that is not ablated (i.e., is imploded) and $(\rho\Delta R)_{0,\text{doped}}$ is the areal density of the doped layer, both in the initial target. The former is known from burnthrough experiments.[7] To demonstrate the validity of this procedure we show in Fig. 79.25(a) the *LILAC*-calculated ratio $R = \rho\Delta R$(shell)/$\rho\Delta R$(doped layer) as a function of time for various separations *S* of the doped layer from the inner shell surface (in the original target). For each curve the target is that of shot 13151, except that *S* was assigned a different value in each case. The calculated shell $\rho\Delta R$ is also shown (the peak $\rho\Delta R$ is ~0.5 g/cm^2). During the first 3 ns of the pulse the ratio *R* decreases because of ablation but during the following compression, especially for $S \sim 1$ μm, it changes only slightly. Since an outer layer of about 13 μm is ablated in shot 13151, the value of *Q* is ~2.5; as Fig. 79.25(a) shows, when $S \sim 1$ μm, this value, when multiplied by the measured doped-layer $\rho\Delta R$, would yield the correct total shell $\rho\Delta R$ at peak compression. Thus, for targets with $S < 1$ μm the procedure would overestimate the total shell $\rho\Delta R$, whereas for $S > 1$ μm it would underestimate it. We further calculate *R* by a model that assumes a constant-density shell that converges radially without compression. Figure 79.25(b) shows the results as a function of the compression ratio; the various curves correspond to the curves of Fig. 79.25(a). The initial target in Fig. 79.25(b) is a 12-μm-thick shell, which corresponds to the unablated target in shot 13151. As seen, the corresponding curves in the two figures are very similar, even though the $\rho\Delta R$ values in the incompressible model are much smaller than in the *LILAC* calculations. This indicates that the procedure is insensitive to the details of the implosion.

The separation of the doped layer in the targets listed in Table 79.III is larger than the optimal; thus, this method will underestimate the total shell $\rho\Delta R$ by about a factor of 2. Since

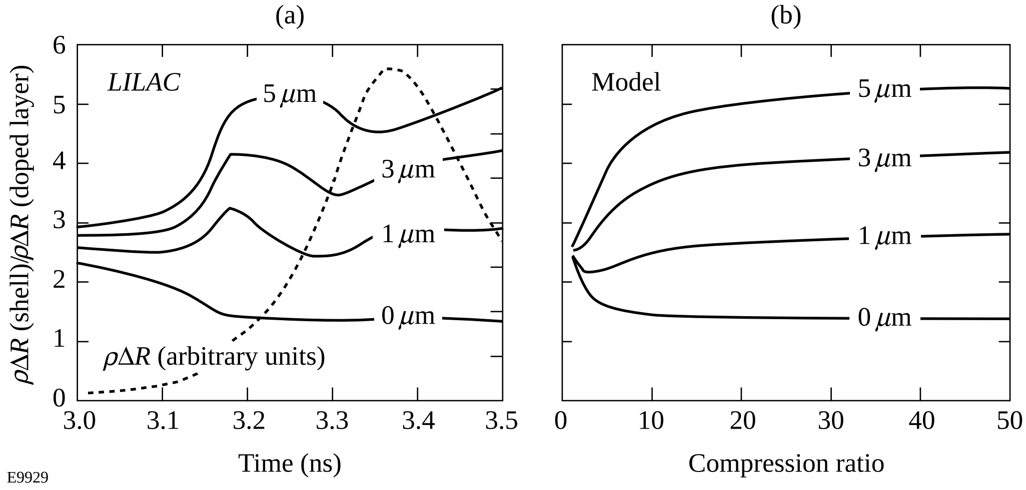

Figure 79.25
The calculated ratio $R = \rho\Delta R(\text{shell})/\rho\Delta R(\text{doped layer})$ for various separations S of the doped layer from the inner shell surface (in the original target). (a) *LILAC*-calculated R as a function of time; the curves correspond to shot 13151 except that S is different for each curve. The calculated shell $\rho\Delta R$ is also shown. (b) Model-calculated R as function of compression ratio; the initial target is assumed to correspond to shot 13151 after the ablation (of 13 μm CH) has been completed.

the value of Q is ~2.5 for the shots of Fig. 79.23 and accounting for this factor-of-2 underestimate, the total shell $\rho\Delta R$ is found to be 70 mg/cm^2 for shot 13151 and 45 mg/cm^2 for shot 13152. The peak shell $\rho\Delta R$ simulated by the 1-D code *LILAC* is ~500 mg/cm^2. This value is higher by a factor of ~7 than what was measured on shot 13151 (with SSD) and by a factor of ~11 on shot 13152 (without SSD). On the other hand, *ORCHID* simulations yield a peak total $\rho\Delta R$ of ~100 mg/cm^2, which is much closer to the experimental value. Further comparisons between the experimental results and code simulations are given below.

The areal-density values obtained above assume a uniform $\rho\Delta R$ over the shell surface. For a shell with modulations in $\rho\Delta R$, *the value* $\rho\Delta R_M$ *measured by opacity will always underestimate the average* $<\rho\Delta R>$ because low-opacity regions have more weight in an integral opacity measurement. For example, if we assume that a fraction α of the shell area consists of radial holes (i.e., opacity $\tau = 0$) and the rest has a constant opacity τ, we find

$$\rho\Delta R_M \big/ \langle \rho\Delta R \rangle = -\ln\left[\alpha + (1-\alpha)\exp(-\tau)\right] \big/ (1-\alpha)\tau, \quad (1)$$

which is always less than 1. Also, it can be shown that for a given measured opacity τ_M, the relation $\alpha < \exp(-\tau_M)$ holds. In Fig. 79.23 the opacity of the absorption lines reaches the value 1.6 from which it follows that $\alpha < 0.2$. In the last section we describe a method for actually measuring the modulations in the areal density of the shell.

The Temperature of the Compressed Shell

The temperature of the shell at peak compression is an additional important parameter characterizing the implosion. We first use the absorption lines in Fig. 79.23 to deduce the temperature of the cool layer. These absorption lines each correspond to a Ti ion with an increasing number of L-shell vacancies; thus, the intensity distribution within the absorption-lines manifold corresponds to a distribution of ionization states from Ti^{+13} to Ti^{+20}. This distribution depends mostly on the temperature but also on the density. We use the collisional-radiative code *POPION*[10] to calculate the distribution of Ti ionization states as a function of temperature and density (for the experimental case of a 6% atom concentration of Ti in CH). Figure 79.26 shows as an example the average charge Z of Ti ions as a function of temperature for two density values: 1 g/cm^3 and 10 g/cm^3. As shown later, the shell density at peak compression is found to be within this range. *POPION* calculations show that for densities within this range, the measured absorption-line intensity distribution indicates a temperature in the range ~250 to ~350 eV. Additionally, the absorption-line intensity distribution is actually wider than that calculated for any single temperature, indicating absorption over a temperature gradient. Including this effect, the total range of possible temperatures indicated by the absorption lines is ~200 to ~400 eV.

We next turn to the determination of the cold-shell temperature. Unlike the cool layer where absorption lines are formed, no absorption lines are available for measuring the temperature of the cold shell (where there are no *L*-shell vacancies into which absorption can take place). Instead, we can use the fluorescent Kα lines that are emitted following photoionization of *K*-shell electrons. To observe these lines more readily we use an off-center view that misses the core emission. We show in Fig. 79.27 the spectrum for shot 13151 in two views: through the center of the target and off the center. Indeed, the off-center view reveals a fluorescent Kα line emitted by *F*-like ions, coinciding in energy with the lowest-energy, *F*-like absorption feature. In the axial view this fluorescence cannot be seen because of the overlapping absorption at the same energy. For a colder shell the Kα line would appear at a slightly lower-energy position, indicating ionization of *M*-shell but not of *L*-shell electrons (the lowest-energy, or cold, Kα line is at 4.508 keV). In that case the Kα line would appear even in the axial view, not being subject to absorption, as has been the case in thicker-shell implosions.[3] The *F*-like Kα line is emitted following the *K*-shell photoionization of the Ne-like ions; thus, the bulk of the cold layer is in the closed-shell, Ne-like state; however, the width of the Kα line indicates that a smaller fraction of the Ti ions may be in lower ionizations. Using this result and *POPION* calculations we estimate the temperature of the cold shell as T ~150 to ~250 eV. For shot 13152 (without SSD) the cold-shell temperature is essentially the same.

It should be noted that in addition to the Kα line emitted in the cold shell, fluorescent Kα lines corresponding to each of the absorption lines of Fig. 79.27 should also be emitted within the cool layer. They cannot be seen in the spectrum because the $\rho\Delta R$ associated with each species having *L*-shell vacancies is only a fraction of the total cool-shell $\rho\Delta R$, which in turn is smaller than the cold-shell $\rho\Delta R$.

The position of the *K* edge can in principle provide an additional signature of the cold-shell temperature because for successive ionizations the *K* edge shifts to higher energies (see Fig. 72.8 in Ref. 2). For Ne-like Ti ions the *K*-edge shift is ~300 eV. This shift, however, is calculated for an isolated ion; at high densities *the K edge shifts to lower energies* due to interaction with neighboring ions. Using the model of Stewart and Pyatt,[11] assuming T ~ 200 eV and a density that changes over the range of 1 to 10 times solid density, the *K* edge of Ne-like Ti should shift toward lower energies by ~120 to ~300 eV; thus, the two effects partly cancel each other. Indeed, no significant *K*-edge shift is seen in Fig. 79.23. Accordingly, the *K*-edge shift is not a very useful diagnostic of shell temperature.

Kα Imaging of the Cold Shell

Previously we have shown that Kα emission constitutes an image of the cold shell around the time of peak compression.[3,5] Using this method we show here that shell compression improves with the implementation of SSD. In Ref. 5 a pinhole-array spectrometer was used to obtain two-dimensional images, whereas here a slit spectrograph is used to obtain essentially one-dimensional images; for shaped-pulse implosions the core

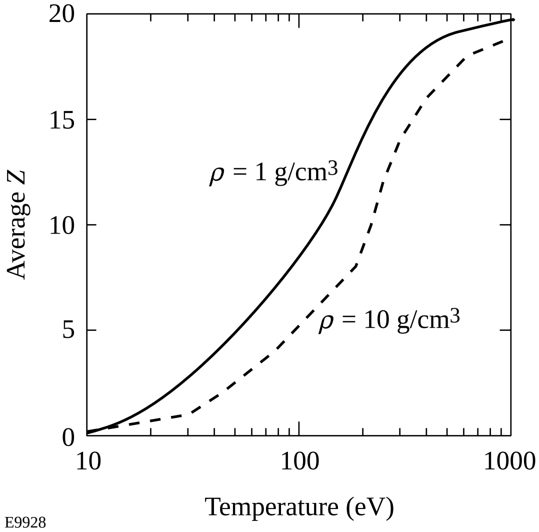

Figure 79.26
The average charge Z of Ti ions as calculated by the collisional-radiative code *POPION*. It is assumed that the titanium forms a 4% mixture (by atom) in CH.

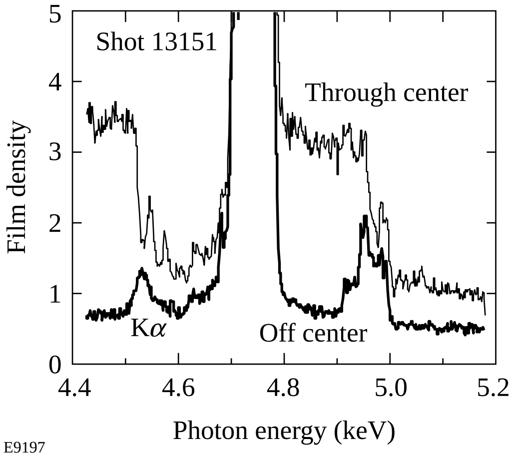

Figure 79.27
Determination of the cold-shell temperature through the fluorescing Kα lines. Only a view off the target center clearly shows the fluorescing line; its state of ionization (*F*-like Ti) indicates a cold-shell temperature of ~200 eV.

images are typically too weak to obtain high-quality images with the former instrument. In Fig. 79.28 we show part of the image obtained with the spatially resolving spectrograph, on two comparable shots, with and without SSD. The slit provides one-dimensional resolution in the vertical direction. In addition, the crystal provides low spatial resolution in the direction of dispersion (due to the Bragg's law); thus, the emission of Ti lines caused by burnthrough, because of their large extent, appears as two-dimensional images. This is important for separating Kα emission pumped by coronal radiation traveling inward during laser irradiation from Kα emission pumped by core radiation traveling outward during peak compression (Kα lines can only be emitted following pumping by a source located in a hotter region). The images of the Ti Heα line and its nearby satellites are elliptically shaped because there is no magnification in the direction of dispersion, whereas magnification in the perpendicular direction is provided by the slit. As in the spectra of Fig. 79.23, we see a much higher intensity of burnthrough radiation (e.g., the Ti Heα lines) in the no-SSD case, indicating a faster (and thus deeper) burnthrough due to instability growth. In fact, the Ti Heα line and its satellites appear as three limb-effect rings in the upper spectrum but are totally saturated in the lower spectrum. The lower spectrum also shows ring images of shifted Kα lines in the range of 4.6 to 4.7 keV. Their size is slightly smaller than that of the Ti Heα rings, indicating that they are pumped by radiation from the burnthrough region during the laser irradiation (see Fig. 75.30 in Ref. 12 and discussion thereof). The species emitting these lines are of relatively high ionization (e.g., B-like and Be-like Ti), indicating that radiation emitted during the burnthrough preheats the outer layer of the cold shell, ahead of the heat front, to ~300 to ~600 eV. These ring images show that *the accelerating shell does maintain its integrity with no large-scale breakup seen*. Such images can be used to study the uniformity of the accelerating shell. As in these target shots, the doping level can be made low enough so as not to greatly modify the behavior of the target and the doped layer can be placed deep enough that a burnthrough occurs at the end of the laser pulse. In this way the radiation from the doped layer does not interfere with the laser interaction and acceleration that occur earlier. *The radiation from the burnthrough thus provides a "flash" photography of the shell at the end of the acceleration phase.*

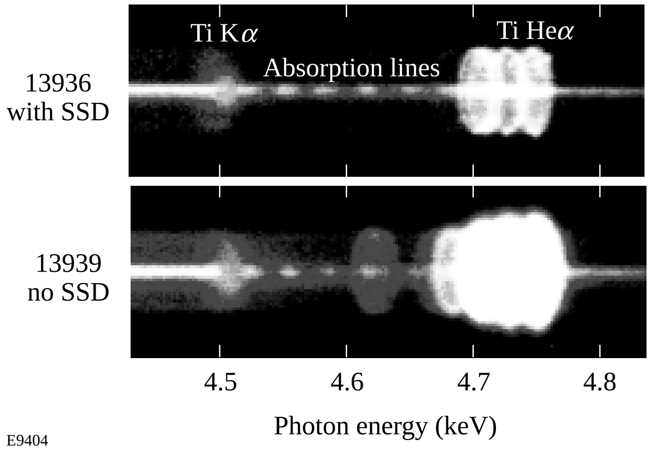

Figure 79.28
Effect of SSD as evidenced by x-ray spectra. A slit provides one-dimensional spatial resolution in the vertical direction; the crystal provides a low spatial resolution in the dispersion direction. Low-temperature Kα line (at ~4.52 keV) is pumped by core radiation; higher-temperature Kα lines (4.6 to 4.7 keV) are pumped by burnthrough to the Ti-doped layer.

In addition to these emission rings of Kα lines, a much stronger Kα line seen at ~4.52 keV (similar to that in Fig. 79.27) is emitted around the core and is clearly pumped by core radiation. The Kα lines are difficult to see in the streak spectra (which would further prove this point) because the integration over the target volume precludes an off-center view; on the other hand, the emission of the cold Kα line at peak compression was previously observed in streak data[5] because, as explained above, it is not absorbed in the shell. Also, related simulations described in Ref. 12 (Fig. 75.30) strongly support this conclusion. The temperature indicated by this feature has been estimated above to be ~150 to ~250 eV. Thus, the outer part of the doped layer is heated by the laser burnthrough to a temperature >1 keV (sufficient to excite Ti^{+20} and Ti^{+21} lines); radiation from this heated region flows inward and causes heating of additional material to ~300 to ~600 eV, all of which is ablated. The bulk of the doped layer, however, remains colder and implodes, reaching temperatures of ~150 to ~250 eV at peak compression. It should be noted that most of the radiative preheating is caused by sub-keV radiation whose range is smaller than the areal density of the initially ~5-μm-thick doped layer. Vertical lineouts through the Kα feature at ~4.52 keV have been Abel inverted,[13] separately for the two branches above and below the core image. The results (Fig. 79.29) clearly show that SSD smoothing results in both *a higher convergence and a higher shell compression*. This is consistent with the conclusion from Fig. 79.23 that SSD smoothing leads to a higher shell $\rho\Delta R$.

The Kα profiles in Fig. 79.29 can be converted to density profiles by requiring that the integral of the normalized profiles yields the measured $\rho\Delta R$ of the doped layer. Using this procedure we obtain peak density of ~1.2 g/cm^3 for shot 13936 and

~0.5 g/cm^3 for shot 13939. These values underestimate the density because time integration broadens the Kα spatial profiles. On the other hand, if the opacity above the *K* edge is much larger than 1, the Kα profile will be narrower than the density profile because of depletion of the pumping radiation; this is not the case in the present results.

1-D *LILAC* and 2-D *ORCHID* Simulations

The shots listed in Table 79.III were simulated with both the 1-D code *LILAC* and the 2-D code *ORCHID*. Present low-adiabat, shaped-pulse implosions perform below 1-D predictions (even with SSD),[14] and their replication is a stringent test for 2-D simulations. A particularly sensitive parameter characterizing target performance is the density profile of the cold shell around peak compression. As explained above, this density profile is determined by normalizing the Ti Kα fluorescence profiles (Fig. 79.29) to the shell $\rho\Delta R$ as measured by the *K*-edge absorption and the 1*s*–2*l* absorption lines. These profiles correspond to the part of the shell that is both doped and cold. As noted above, the target parameters were chosen so that all of the cold shell at peak compression would be doped so the Kα profile would correspond to the entire cold shell. Since we observe burnthrough of the laser into the doped layer (see Figs. 79.23 and 79.28), we can safely assume that none of the CH overcoat is cold during the compression. In Fig. 79.28, in addition to the ring-shaped images of the Ti Heα line at 4.75 keV (and its nearby satellites), a strong emission of these lines is also seen at the center of the target. To see this more clearly, we show in Fig. 79.30 the spatial profile of the calibrated intensity at the energy of the Ti Heα line, and at a nearby energy of the continuum; comparing the two lineouts clearly indicates a strong central emission of the Ti Heα line. Thus, the inner part of the doped layer must be part of the hot core, and the cold part of the shell contains only doped material. If the shell becomes highly distorted during either the acceleration or the deceleration, some of the Ti Heα emission may be due to mixing; in this case, some of the cold material will be undoped and the measured $\rho\Delta R$ through Ti absorption will underestimate the true cold-shell $\rho\Delta R$.

ORCHID simulations include the imprint of laser nonuniformity. For each beam, the known mode spectrum due to the phase plates was used, and modes up to $\ell = 300$ were added with random relative phases. The effect of multiple-beam overlap was calculated separately and accounted for. The effect of SSD was simulated by randomly reversing the phase of the laser modes at intervals equal to the coherence time (which is inversely proportional to the bandwidth and decreases with increasing mode number). Figure 79.31(a) shows typical profiles, azimuthally averaged, at peak compression; the averaged temperature was weighted by the density. A hot core is seen to be surrounded by a dense, colder layer. Before

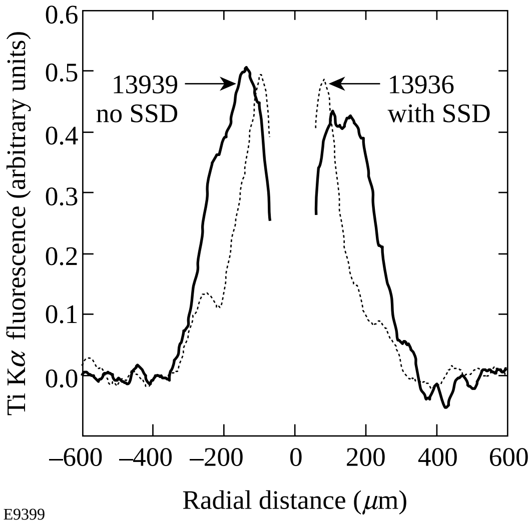

Figure 79.29
Abel inversion of image lineouts (from Fig. 79.28) at the *F*-like Kα line. The curves delineate the position and thickness of the cold shell around the time of peak compression. Higher convergence and compression due to SSD smoothing are evident.

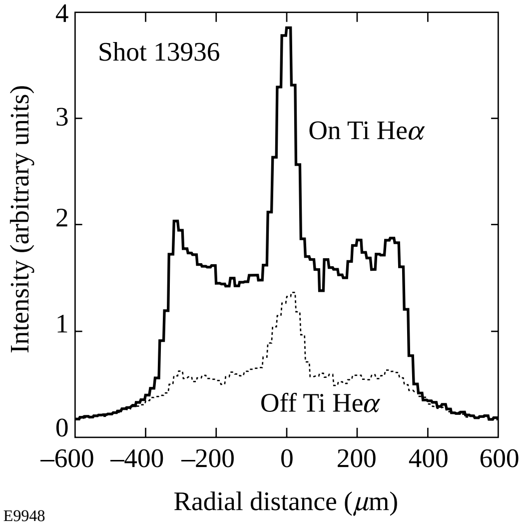

Figure 79.30
Spatial profile of the intensity at the energy of the Ti Heα line and at a nearby energy of the continuum (shot 13936) showing central emission of the line. This demonstrates that the cold shell around peak compression, detected by absorption, is mostly titanium doped.

comparing the *ORCHID* results to the experiment we note that the Ti Kα emission measures only the cold part of the shell. More specifically, the Kα line was shown in Fig. 79.27 to be emitted by neon-like and possibly lower ionizations. Thus, the density profile measured by the Kα line fluorescence refers only to that part of the total density that is cold enough to have a charge state $Z \leq 12$. To compare the *ORCHID* density profiles to the experiment we multiply the former by the fraction of Ti ions in charge states $Z \leq 12$, calculated by the collisional-radiative *POPION* code.[10] For the most part, the Ti in these calculations is in the neon-like state with only a small contribution from lower ionizations. In Fig. 79.31(b) we show typical cold-shell density profiles obtained in this way at three times around peak compression. Finally, to allow for comparison with the time-integrated Kα profiles, we calculate the time-averaged *ORCHID* density profile. We note that the Kα line intensity is proportional to the intensity of pumping core radiation (in addition to being proportional to the cold-shell $\rho\Delta R$ or, after Abel inverting, to ρ). Therefore, the average density profile was obtained by weighting the instantaneous density profiles by the core intensity just below the Ti *K* edge, obtained from the streak spectrograph data. Good agreement is seen in *both the shape and absolute magnitude* of the two density profiles: the time-averaged *ORCHID* profile and the profile measured through the Ti Kα fluorescence. On the other hand, the 1-D code *LILAC* shows a much narrower profile of vastly higher density (most of the sharp density peak in that profile is cold and should have been measured by the Kα profile in a 1-D implosion).

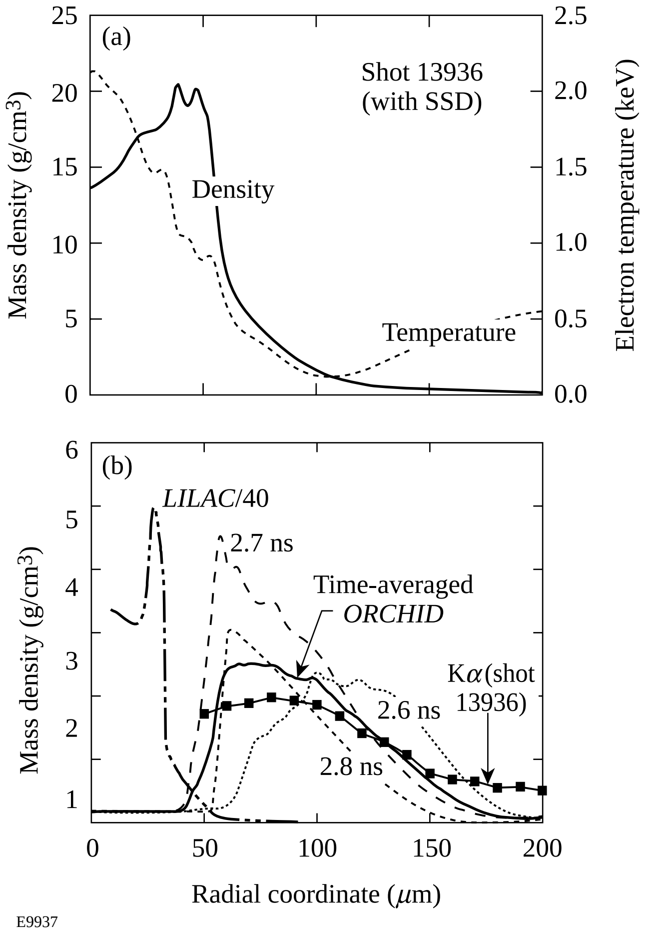

Figure 79.31
(a) Azimuthally averaged density and electron temperature profiles at peak compression calculated by *ORCHID* for shot 13936 (with SSD). (b) Density profiles of the cold shell for shot 13936. The 1-D *LILAC* profile shown is at peak compression. Three typical 2-D *ORCHID* profiles during different times of the compression are also shown. Using such profiles, the time-averaged density profile was obtained, weighted by the core intensity. The experimental time-integrated cold-shell density profile was obtained from the Ti Kα image.

In spite of the inherent inaccuracies in both the experiment and simulations, Fig. 79.31 shows that the cold-shell imaging diagnostics employed here provides a sensitive signature for testing the performance of 2-D codes in simulating unstable implosions. Further comparisons of measured and *ORCHID*-calculated modulations in compressed-shell $\rho\Delta R$ are underway.

Measurement of Shell $\rho\Delta R$ Modulation Through *K*-Edge Imaging

In addition to the integral measurements of shell $\rho\Delta R$ described above, we introduce a new method for *imaging the shell* $\rho\Delta R$ at peak compression, effectively using the core radiation as a backlighter for the shell. Such images are the final product of shell deformation due to the Rayleigh–Taylor instability and the Bell–Plesset effect and are thus of great interest in laser-fusion studies. Spatial modulations in a core image viewed through an absorbing shell depend on both the modulations in core emission as well as the modulations in shell $\rho\Delta R$. To isolate the latter, we use targets with a Ti-doped layer embedded within the shell and take the ratio of an image $I_{<K}$ just below the Ti *K* edge (at 4.96 keV) and an image $I_{>K}$ just above it. Since the absorption $\mu_{>K}$ above the *K* edge is much higher (by a factor of ~9.5) than the absorption $\mu_{>K}$ below it, the $\rho\Delta R$ image can be obtained through

$$\rho\Delta R = \ln\left(I_{<K}\right) / I_{>K} / \left(\mu_{>K} - \mu_{<K}\right). \qquad (2)$$

The method relies on the fact that the emitted continuum intensity (before absorption) changes very little between the two images. The thickness and doping level of the doped layer can be conveniently adjusted to result in an opacity $\rho\Delta R\ \mu_{>K}$ ~1 to 2.

A particularly convenient way of obtaining such images is by employing the recently developed pinhole-array spectrometer.[5] Several hundred narrow-bandwidth images in the range of ~4 to ~7 keV are obtained at ~10-eV energy shifts between adjacent images. This device is particularly useful for *K*-edge imaging because monochromatic images provide high sensitivity to $\rho\Delta R$ modulations; also, the large number of images obtained close to either side of the *K* edge enables an improved noise analysis and consistency checks.

As a first test of the proposed method we applied it to an implosion (shot 15156) using a 1-ns square laser pulse. This choice was made because fast-rising pulses produce more-intense core radiation. The target and laser conditions are listed on the last line in Table 79.III. We use a pinhole-array spectrometer with 10-μm holes, giving a spatial resolution of ~16 μm. Figure 79.32 shows part of the image around the Ti *K* edge (4.964 keV); the crystal dispersion is in the horizontal direction. Each image is a monochromatic image of the core (of ~100-μm diameter), at a slightly different energy. In the vertical direction successive images are at energies separated by ~10 eV; in the horizontal (dispersion) direction the separation is ~100 eV. The energy bandwidth for each image is ~5 eV.[5] The six images on the left [Fig. 79.32(a)] are at energies just below the Ti *K* edge; the six images on the right [Fig. 79.32(b)] are just above the edge. The emission from the laser-interaction region is not seen in these images because, unlike the shots shown in Figs. 79.23 and 79.27, there has been no burnthrough to the Ti-doped layer in shot 15156. This is because of the thicker CH overlayer and the shorter laser pulse in this shot. The images below the *K* edge show structure on a scale length of about 20 to 30 μm. The images above the *K* edge show a similar structure. As explained, the structure in images below the edge is caused by nonuniformities in the core emission; the structure in the images above the edge reflects those same nonuniformities, plus any nonuniformities in the $\rho\Delta R$ of the absorbing shell. The purpose of the analysis described here is to separate the two sources of nonuniformity. To that end we perform 2-D Fourier analysis of the images in optical-density units and azimuthally average the results. In most other shots under similar conditions the core emission is more uniform; however, this shot was chosen to test the method's capability. The images in Fig. 79.32 are in optical-depth units [i.e., OD ~ ln(*I*), where the intensity *I* was deduced from the DEF-film density]. First, we must obtain the spatial spectrum of the noise (both in the images and in the film); to that end we subtract the Fourier spectra of two core images at energies below the *K* edge. Since the gross structure in all the images just below the *K* edge is the same, the difference between such images is caused only by the noise. Figure 79.33 shows the noise spectrum (thin solid line) thus obtained as an

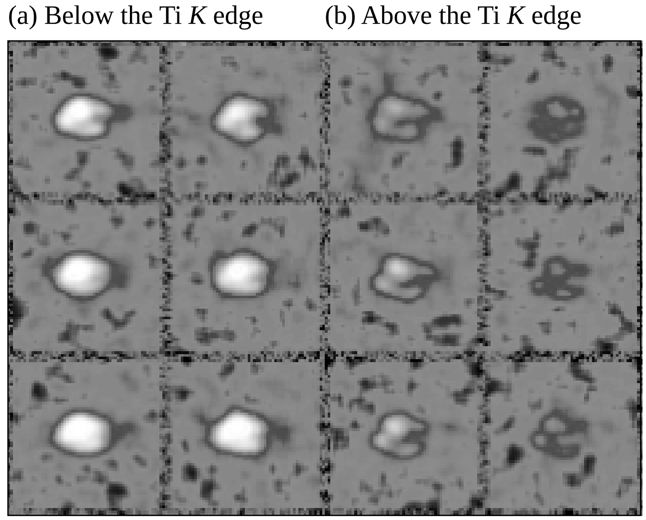

Figure 79.32
Sample of time-integrated monochromatic images of the core radiation obtained with a pinhole-array spectrometer, at energies (a) below the titanium *K* edge and (b) above the titanium *K* edge.

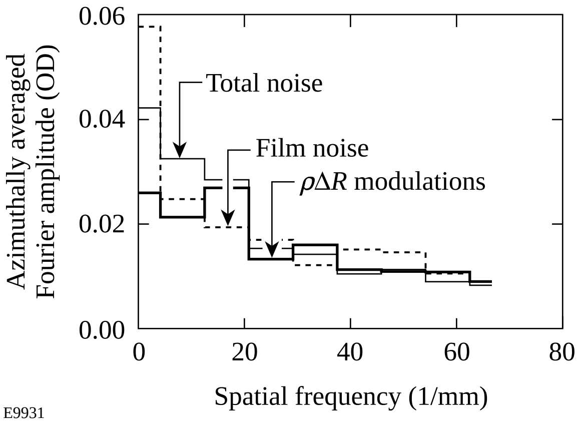

Figure 79.33
The azimuthally averaged Fourier amplitude of the measured optical depth versus spatial frequency for (a) the noise in the images below the *K* edge (thin solid line), (b) the film noise taken in an area between the images (dashed line), and (c) the modulations in $\rho\Delta R$ of the titanium-doped layer (thick solid line).

azimuthally averaged Fourier amplitude of optical-depth modulations versus spatial frequencies, using two of the images shown in Fig. 79.32(a); the results of using different image pairs from the same figure are very similar. The maximum spatial frequency corresponds to the spatial resolution of ~16 μm. Next we deduce the spectrum of film noise by analyzing in the same way a region on the film between the images, of equal area to that of the images; the dashed line in Fig. 79.33 shows the results. Finally, we derive the modulations in shell $\rho\Delta R$ by analyzing the difference in optical depth between two images at energies below and above the K edge. The spectrum of this difference, shown by the thick solid line in Fig. 79.33, contains noise plus modulations in the opacity of the titanium-doped layer. As seen in Eq. (2), the modulations in optical depth are proportional to the areal-density modulations of the doped layer. The three curves in Fig. 79.33 are very close for spatial frequencies above ~10 mm^{-1} or wavelengths shorter than 100 μm (the latter being about equal to the core size), indicating that *the film noise accounts for all the modulations in the images*; thus, there are no measured modulations in the shell areal density above the noise level for wavelengths between ~16 and ~100 μm. The sensitivity of this measurement was estimated using the noise spectrum obtained above. Assuming that modulations of the shell $\rho\Delta R$ are contained in the region of wavelengths from 10 to 80 μm, the σ_{rms} amplitude of the layer modulations must be more than a third of its thickness to become distinguishable from the noise. Thus, this analysis does not show modulations exceeding ~30% in the $\rho\Delta R$ of the doped layer, of wavelengths longer than ~16 μm and smaller than ~100 μm. We attribute this to the fast-rising square laser pulse, which reduces laser imprint and thus target distortions. Slower-rising pulse shapes (such as the ALPHA306 pulse used to obtain Fig. 79.23 data) are known to produce less-stable implosions, but the core intensity in such target shots was insufficient to perform meaningful analysis with this method. In future experiments we plan to increase the sensitivity of the measurement by replacing the diffracting crystal in the pinhole-array spectrometer with filters for sampling the spectrum below and above the Ti K edge. The loss in spectral definition can be partly offset by accounting for the spectrum, independently measured from a target without a doped layer.

ACKNOWLEDGMENT

This work was supported by the U.S. Department of Energy Office of Inertial Confinement Fusion under Cooperative Agreement No. DE-FC03-92SF19460, the University of Rochester, and the New York State Energy Research and Development Authority. The support of DOE does not constitute an endorsement by DOE of the views expressed in this article.

REFERENCES

1. B. Yaakobi, F. J. Marshall, D. K. Bradley, J. A. Delettrez, R. S. Craxton, and R. Epstein, Phys. Plasmas **4**, 3021 (1997).
2. Laboratory for Laser Energetics LLE Review **72**, 168, NTIS document No. DOE/SF/19460-199 (1997). Copies may be obtained from the National Technical Information Service, Springfield, VA 22161.
3. B. Yaakobi and F. J. Marshall, J. Quant. Spectrosc. Radiat. Transfer **61**, 465 (1999).
4. D. K. Bradley, J. A. Delettrez, R. Epstein, R. P. J. Town, C. P. Verdon, B. Yaakobi, S. Regan, F. J. Marshall, T. R. Boehly, J. P. Knauer, D. D. Meyerhofer, V. A. Smalyuk, W. Seka, D. A. Haynes, Jr., M. Gunderson, G. Junkel, C. F. Hooper, Jr., P. M. Bell, T. J. Ognibene, and R. A. Lerche, Phys. Plasmas **5**, 1870 (1998).
5. B. Yaakobi, F. J. Marshall, and D. K. Bradley, Appl. Opt. **37**, 8074 (1998).
6. Laboratory for Laser Energetics LLE Review **37**, 29, NTIS document No. DOE/DP40200-83 (1998). Copies may be obtained from the National Technical Information Service, Springfield, VA 22161.
7. D. K. Bradley, J. A. Delettrez, and C. P. Verdon, Phys. Rev. Lett. **68**, 2774 (1992); J. Delettrez, D. K. Bradley, and C. P. Verdon, Phys. Plasmas **1**, 2342 (1994).
8. D. J. Botto, J. McEnnan, and R. H. Pratt, Phys. Rev. A **18**, 580 (1978).
9. B. Yaakobi, R. S. Craxton, R. Epstein, and Q. Su, J. Quant. Spectrosc. Radiat. Transfer **58**, 75 (1997).
10. R. Epstein, S. Skupsky, and J. Delettrez, J. Quant. Spectrosc. Radiat. Transfer **35**, 131 (1986).
11. J. C. Stewart and K. D. Pyatt, Jr., Astrophys. J. **144**, 1203 (1966).
12. Laboratory for Laser Energetics LLE Review **75**, 182, NTIS document No. DOE/SF/19460-246 (1998). Copies may be obtained from the National Technical Information Service, Springfield, VA 22161.
13. C. M. Vest and D. G. Steel, Opt. Lett. **3**, 54 (1978).
14. Laboratory for Laser Energetics LLE Review **78**, 82, NTIS document No. DOE/SF/19460-295 (1999). Copies may be obtained from the National Technical Information Service, Springfield, VA 22161.